Half-integer quantized thermal conductance plateau in chiral topological superconductor systems

Ning-Xuan Yang,[1] Qing Yan,[2] and Qing-Feng Sun[2,3,4,*]

[1]*Department of Physics, College of Sciences, Shihezi University, Shihezi 832000, China*

[2]*International Center for Quantum Materials, School of Physics, Peking University, Beijing 100871, China*

[3]*Beijing Academy of Quantum Information Sciences, West Bld.#3, No.10 Xibeiwang East Rd., Haidian District, Beijing 100193, China*

[4]*Collaborative Innovation Center of Quantum Matter, Beijing 100871, China*

(Received 27 November 2021; accepted 4 March 2022; published 18 March 2022)

We investigate the thermal transport properties of a quantum anomalous Hall insulator nanoribbon covered by superconductors. Due to the peculiar properties of chiral Majorana fermion (CMF) edge states, we found a half-integer quantized thermal conductance plateau. Different from the ordinary superconductor which conducts electricity but does not conduct heat, in the quantum anomalous Hall insulator–topological superconductor junction, the CMF occurs at the boundary of the topological superconductor which carries heat from left to right. A chiral topological superconductor with Chern number $\mathcal{N} = \pm 1$ has a single CMF, which is equivalent to half an ordinary fermion propagating along the edge, leading to a half-integer quantized thermal conductance plateau. When the topological superconducting edge has two CMFs, it is equivalent to ejecting an ordinary fermion, resulting in an integer quantized thermal conductance plateau. Moreover, the half-integer quantized thermal conductance can also be used to study the properties of Majorana Kramer pairs in a helical topological superconductor. Finally, we also find that the half-integer quantized plateau appears against moderate disorder and with the metal leads besides the quantum anomalous Hall insulator, which is promising to be realized in experiments.

DOI: 10.1103/PhysRevB.105.125414

I. INTRODUCTION

Eighty-five years ago, Majorana discovered a charge-neutral fermion when solving the relativistic wave equation of electrons. Its antiparticle is itself called Majorana fermion [1,2]. Over 10 years, Majorana fermions have attracted much attention in the field of condensed-matter physics [3–8]. The detection and regulation of Majorana fermions are not only helpful to satisfy the basic theoretical research, but also pave the way to realize topological quantum computation because of the statistical properties of a Majorana fermion under exchange operations [9–13].

The chiral topological superconductors (TSC) are a new topological physical state with a pairing gap in the bulk and gapless edge modes consisting of a chiral Majorana fermion (CMF) state [4]. It can be realized by the quantum anomalous Hall insulator (QAHI) covered by the *s*-wave superconductor via the proximity effect [7,14–22]. One-dimensional CMFs exist at the boundary of two-dimensional chiral TSC [4,14,15]. The CMFs can perform the non-Abelian braiding and are also expected to realize topological quantum computation [9,10,23,24]. Therefore, CMF has gained much attention in recent years [2,5–7,14–22,25–30]. So far, detecting the existence of the Majorana edge states is a very challenging work in experiments. Although one experiment claimed the half-quantized electric conductance in a hybrid QAHI-TSC-QAHI system to confirm the chiral Majorana edge modes [25], subsequent theoretical and experimental interpretations [26–30] seem to show alternative origins of the half-quantized conductance plateau, such as the percolation of QAH edges induced by magnetic disorder in the QAHI, or the device being in two QAH states with well-aligned magnetization. Therefore, more evidence is needed for the existence of a single CMF in a hybrid QAHI-TSC-QAHI structure.

Similar to electronic transport, thermal transport is also an effective way to reveal the intrinsic physics of quantum channels. The quantized thermal conductance, $\kappa_e/\mathcal{T} = g\frac{\pi^2 k_B^2}{3h}$, denotes the single quantum channel in quantum point contact [31–33]. However, up to now, no investigations of the thermal transport of a hybrid QAHI-TSC-QAHI system have been reported. At first glance, the physical realization of CMF in a hybrid QAHI-TSC-QAHI system is based on TSCs. In TSCs, both the Cooper pair and the CMF can carry current. Due to the interference of the Cooper pair, it is usually difficult to characterize CMFs simply by electronic transport. In ordinary superconductors, electrons are condensed into Cooper pairs and do not conduct heat. However, in the TSCs, heat can be carried by chiral Majorana edge states, which avoids the influence of Cooper pairs. Therefore, the detection of charge-neutral CMFs by thermal transport has obvious advantages.

In this paper, based on the Landauer-Büttiker formula, we investigate the properties of thermal transport of CMF edge states in a hybrid QAHI-TSC-QAHI (or metal-TSC-metal) nanoribbon junction [see Fig. 1(a)] and find the half-quantized thermal conductance plateau. The unique phenomenon of the half-quantized plateaus originates from the peculiar properties

*sunqf@pku.edu.cn

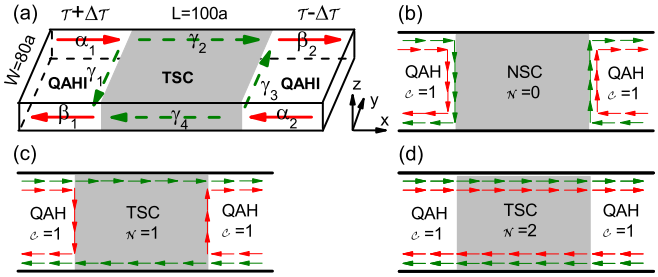

FIG. 1. (a) Schematic diagram of a hybrid QAHI-TSC-QAHI structure connected to a hot and a cold lead. A thermal gradient $2\Delta\mathcal{T}$ is applied in x direction. (b)–(d) The edge transport configurations of the hybrid QAHI-SC-QAHI structure with the topological Chern number of the SC region being $\mathcal{N} = 0, 1, 2$, respectively.

of CMFs in chiral TSC with Chern number $\mathcal{N} = \pm 1$. The quantized thermal conductance plateaus can well remain in a certain temperature range and moderate disorder. This significant feature of the half-quantized thermal conductance plateau can be used as a smoking-gun signature to detect CMFs in the experiment.

The rest of the paper is organized as follows. In Sec. II, the effective tight-binding Hamiltonian including QAHI and TSC is introduced. The formalisms for calculating electric thermal conductance are then derived. In Sec. III, we study the thermal transport properties of the hybrid QAHI-TSC-QAHI and metal-TSC-metal system. In Sec. IV, we study the thermal transport in helical TSC. In Sec. V, the effect of disorder on the thermal conductance plateau is investigated. Finally, discussion about the experimental realization and a brief summary are shown in Sec. VI.

II. MODEL AND METHODS

A. Model and Hamiltonian

Considering the low-energy state, the effective Hamiltonian of a QAHI thin film [15,17,21,34,35] can be written as $\mathcal{H}_{\rm QAHI} = \Sigma_{\mathbf{p}} \psi^{\dagger}_{\mathbf{p}} H_{\rm QAHI}(\mathbf{p}) \psi_{\mathbf{p}}$, with $\psi_{\mathbf{p}} = (c^{t}_{\mathbf{p}\uparrow}, c^{t}_{\mathbf{p}\downarrow}, c^{b}_{\mathbf{p}\uparrow}, c^{b}_{\mathbf{p}\downarrow})^{T}$, and

$$H_{\rm QAHI}(\mathbf{p}) = v_F(p_y\tau_z\sigma_x - p_x\tau_z\sigma_y) + m(\mathbf{p})\tau_x\sigma_0 + M_{\rm QAHI}\tau_0\sigma_z - \mu_{\rm QAHI}\tau_0\sigma_0, \quad (1)$$

where $(\sigma_x, \sigma_y, \sigma_z)$ and (τ_x, τ_y, τ_z) are Pauli matrices for the spin and layer spaces, respectively. $c^{t(b)}_{p\sigma}$ and $c^{t(b)\dagger}_{p\sigma}$ are annihilation and creation operators with momentum $\mathbf{p} = (p_x, p_y)$ and spin $\sigma = \uparrow, \downarrow$ in the top (bottom) layer. $m(\mathbf{p}) = m_0 - m_1(p_x^2 + p_y^2)$ describes the coupling between the top and bottom layers. In the calculation, we set the parabolic term $m_0 = -0.1$ and $m_1 = 1$, and the Fermi velocity $v_F = 1$ [15,21,34]. $M_{\rm QAHI}$ represents the exchange field along the z direction to destroy the time-reversal symmetry. The change in $M_{\rm QAHI}$ can drive a phase transition from a trivial insulator with the Chern number $\mathcal{C} = 0$ ($|M_{\rm QAHI}| < |m_0|$) to a QAH state with $\mathcal{C} = \pm 1$ ($|M_{\rm QAHI}| > |m_0|$) [15,21]. $\mu_{\rm QAHI}$ describes the chemical potential. By adjusting $\mu_{\rm QAHI}$, the QAH system can be placed in the metallic phase with $|\mu_{\rm QAHI}| > |m_0|$ [14].

When in proximity to the s-wave superconductor, a finite pairing potential is induced in the QAHI and the

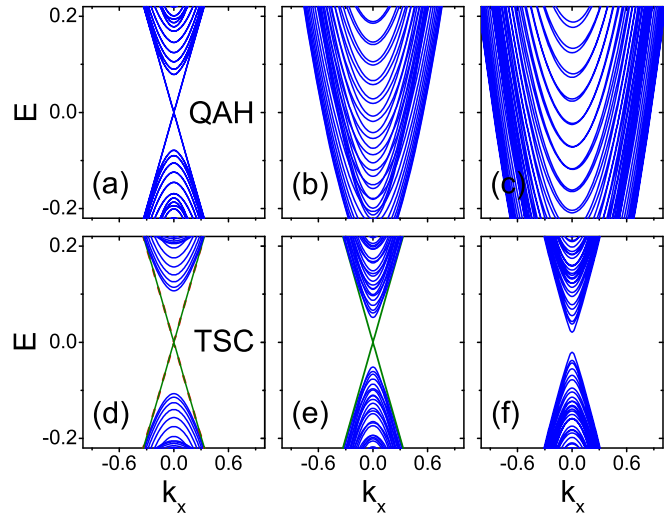

FIG. 2. (a)–(c) Band structure of the QAHI nanoribbon with exchange field $M_{\rm QAHI} = 0.25$, chemical potential $\mu_{\rm QAHI} = 0$ (a), $\mu_{\rm QAHI} = 0.8$ (b), and $\mu_{\rm QAHI} = 1.5$ (c). (d)–(f) Band structure of the TSC nanoribbon; the pairing potentials of the top and bottom layers are $\Delta^t = 0.2$ and $\Delta^b = 0$. Exchange field $M_z = 0.45$ in TSC with Chern number $\mathcal{N} = 2$ (d), $M_z = 0.15$ with $\mathcal{N} = 1$ (e), and $M_z = 0.02$ with $\mathcal{N} = 0$ (f).

Bogoliubov–de Gennes (BdG) Hamiltonian [15,17,21,34] with $\Psi_{\mathbf{p}} = [(c^{t}_{\mathbf{p}\uparrow}, c^{t}_{\mathbf{p}\downarrow}, c^{b}_{\mathbf{p}\uparrow}, c^{b}_{\mathbf{p}\downarrow}), (c^{t\dagger}_{-\mathbf{p}\uparrow}, c^{t\dagger}_{-\mathbf{p}\downarrow}, c^{b\dagger}_{-\mathbf{p}\uparrow}, c^{b\dagger}_{-\mathbf{p}\downarrow})]^{T}$ can be written as $\mathcal{H}_{\rm BdG} = \frac{1}{2}\Sigma_{\mathbf{p}}\Psi^{\dagger}_{\mathbf{p}} H_{\rm BdG}(\mathbf{p})\Psi_{\mathbf{p}}$,

$$H_{\rm BdG} = \begin{pmatrix} H_{\rm QAHI}(p) & \Delta_0 \\ \Delta_0^{\dagger} & -H^{*}_{\rm QAHI}(-p) \end{pmatrix}, \quad (2)$$

where

$$\Delta_0 = \begin{pmatrix} i\Delta^t\sigma_y & 0 \\ 0 & i\Delta^b\sigma_y \end{pmatrix}. \quad (3)$$

Here, Δ^t and Δ^b are the pairing potentials of the top and bottom layers, respectively. To distinguish between the exchange field of QAHI region, M_z represents the exchange field strength of TSC, which is equal to $M_{\rm QAHI}$ in Eq. (1). As M_z increases, the system goes through a series of topological phase transitions from Chern number $\mathcal{N} = 0$ to $\mathcal{N} = 1$ and then to $\mathcal{N} = 2$ with inequivalent $\Delta^t \neq \Delta^b$ [15,21,34]. The phase boundary can be expressed as $\mp(\Delta^t \cdot M_z - \Delta^b \cdot M_z) + M_z^2 = m_0^2 + \Delta^t \cdot \Delta^b$ [15]. The $\mathcal{N} = 0$ phase is a trivial superconducting phase without CMFs, which is denoted as NSC. The $\mathcal{N} = 1$ phase is a TSC with a single chiral Majorana edge state at its edge and the $\mathcal{N} = 2$ phase is topologically equivalent to the $\mathcal{C} = 1$ QAH state with two chiral Majorana edge states [15,21,34] [see Figs. 1(b)–1(d)]. We also plot the band structure of QAHI and TSC to clearly illustrate the edge states; see Fig. 2. Figures 2(a)–2(c) show the band structure of the QAHI nanoribbon. Among them, Fig. 2(a) corresponds to the energy-band structures of the QAH state with $\mathcal{C} = \pm 1$, where the two chiral Dirac edge states crossing the bulk gap intersect at $E = 0$ and Figs. 2(b) and 2(c) correspond to the energy-band structures of a metallic phase with $\mu_{\rm QAHI} = 0.8$ and 1.5. Figures 2(d)–2(f) show the band structure of the TSC nanoribbon. In Fig. 2(d), $\mathcal{N} = 2$ chiral TSC has two

degenerate edge states intersecting in the bulk band gap. $\mathcal{N}=1$ chiral TSC has a single edge state in the bulk gap; see Fig. 2(e). For $\mathcal{N}=0$ trivial superconductors, there is no edge state in the bulk gap [see Fig. 2(f)].

Due to the existence of the superconductor, when an incident electron with the energy E flows from the left QAHI terminal into the central TSC region, there are four processes [17,19,22], which are the normal tunneling, the local Andreev reflection (*LAR*), the crossed Andreev reflection (*CAR*), and normal reflection. Corresponding transmission coefficients can be obtained by using the nonequilibrium Green's function method [17,19,22]:

$$T(E)=\mathrm{Tr}\left[\Gamma^L_{ee}G^r_{ee}\Gamma^R_{ee}G^a_{ee}\right], \tag{4}$$

$$T_{\mathrm{LAR}}(E)=\mathrm{Tr}\left[\Gamma^L_{ee}G^r_{eh}\Gamma^L_{hh}G^a_{he}\right], \tag{5}$$

$$T_{\mathrm{CAR}}(E)=\mathrm{Tr}\left[\Gamma^L_{ee}G^r_{eh}\Gamma^R_{hh}G^a_{he}\right], \tag{6}$$

where e and h represent electron and hole, respectively, and E is the incident energy. $\Gamma^{L/R}(E)=i[\Sigma^r_{L/R}-\Sigma^a_{L/R}]$ is the linewidth function, with the self-energy $\Sigma^r_{L/R}=\Sigma^{a\dagger}_{L/R}$ stemming from the coupling between the left/right (L/R) QAHI leads and the center TSC region. $G^r(E)=[E-\mathcal{H}_{\mathrm{cen}}-\Sigma^r_L-\Sigma^r_R]^{-1}$ is the retarded Green's function with the Hamiltonian $\mathcal{H}_{\mathrm{cen}}$ of the center region [36,37]. In the numerical calculations, we set the nanoribbon width $W=80a$ with the dimensionless lattice constant $a=0.75$ and the central TSC length $L=100a$ throughout this paper unless otherwise mentioned.

B. Electric thermal conductance

After obtaining the transmission coefficients, by using the Landauer-Büttiker formula, the heat current expression can be rewritten as [38–42]

$$\begin{aligned}Q_L=&\frac{1}{h}\int(E-\mu_{\mathrm{L}})T(E)[f_{\mathrm{L}}(E)-f_{\mathrm{R}}(E)]dE\\&+\frac{1}{h}\int(E-\mu_{\mathrm{L}})T_{LAR}(E)[f_{\mathrm{L}}(E)-\widetilde{f}_{\mathrm{L}}(E)]dE\\&+\frac{1}{h}\int(E-\mu_{\mathrm{L}})T_{CAR}(E)[f_{\mathrm{L}}(E)-\widetilde{f}_{\mathrm{R}}(E)]dE,\end{aligned} \tag{7}$$

where $f_\alpha(E)=[e^{(E-\mu_\alpha)/k_B\mathcal{T}_\alpha}+1]^{-1}$ and $\widetilde{f}_\alpha(E)=1-f_\alpha(-E)=[e^{(E+\mu_\alpha)/k_B\mathcal{T}_\alpha}+1]^{-1}$ denote the Fermi-Dirac distribution functions for electrons and holes, respectively. In thermal transport, the temperature difference drives the movement of electric charges. So we set $\mu_{\mathrm{L}}=\mu_{\mathrm{R}}=0$; then

$$\begin{aligned}f_{\mathrm{L}}(E)-f_{\mathrm{R}}(E)&=\frac{1}{e^{E/k_B\mathcal{T}_{\mathrm{L}}}+1}-\frac{1}{e^{E/k_B\mathcal{T}_{\mathrm{R}}}+1},\\f_{\mathrm{L}}(E)-\widetilde{f}_{\mathrm{L}}(E)&=\frac{1}{e^{E/k_B\mathcal{T}_{\mathrm{L}}}+1}-\frac{1}{e^{E/k_B\mathcal{T}_{\mathrm{L}}}+1}=0,\\f_{\mathrm{L}}(E)-\widetilde{f}_{\mathrm{R}}(E)&=\frac{1}{e^{E/k_B\mathcal{T}_{\mathrm{L}}}+1}-\frac{1}{e^{E/k_B\mathcal{T}_{\mathrm{R}}}+1},\end{aligned} \tag{8}$$

and the heat current expression can be written as

$$\begin{aligned}Q_L=&\frac{1}{h}\int E[T(E)+T_{CAR}(E)]\\&\times\left[\frac{1}{e^{\frac{E}{k_B(\mathcal{T}+\Delta\mathcal{T})}}+1}-\frac{1}{e^{\frac{E}{k_B(\mathcal{T}-\Delta\mathcal{T})}}+1}\right]dE,\end{aligned} \tag{9}$$

where $\mathcal{T}_{\mathrm{L}}=\mathcal{T}+\Delta\mathcal{T}$ and $\mathcal{T}_{\mathrm{R}}=\mathcal{T}-\Delta\mathcal{T}$. Assuming small thermal gradient $\Delta\mathcal{T}$, the Fermi distribution function in Eq. (9) can be expanded linearly,

$$\begin{aligned}f(E,\mathcal{T}_{\mathrm{p}})=&\frac{1}{e^{\frac{E}{k_B\mathcal{T}_{\mathrm{p}}}}+1}=f_0+\Delta\mathcal{T}_{\mathrm{p}}\frac{\partial f}{\partial\mathcal{T}_{\mathrm{p}}}\bigg|_{V_{\mathrm{p}}=0,\mathcal{T}_{\mathrm{p}}=\mathcal{T}}\\=&f_0(E)+f_0(E)[1-f_0(E)]\left(\frac{E}{k_B}\right)\frac{\Delta\mathcal{T}_{\mathrm{p}}}{\mathcal{T}^2},\end{aligned} \tag{10}$$

where $p=L,R$. $f_0(E)=[e^{E/k_B\mathcal{T}}+1]^{-1}$ is the Fermi distribution in the zero bias and zero thermal gradient. So,

$$\begin{aligned}Q_L=&\frac{1}{h}\int E^2[T(E)+T_{CAR}(E)]f_0(E)[1-f_0(E)]\\&\times\frac{\Delta\mathcal{T}_{\mathrm{L}}-\Delta\mathcal{T}_{\mathrm{R}}}{k_B\mathcal{T}^2}dE.\end{aligned} \tag{11}$$

The electric thermal conductance is defined as $\kappa_e=\lim\frac{Q_L}{\Delta\mathcal{T}_{\mathrm{L}}-\Delta\mathcal{T}_{\mathrm{R}}}$; then

$$\kappa_e=\frac{1}{h}\int[T(E)+T_{CAR}(E)]f_0(E)[1-f_0(E)]\frac{E^2}{k_B\mathcal{T}^2}dE. \tag{12}$$

As to the contribution from electrons and phonons, the electronic thermal conductance presents a linear relation to the temperature, while the phononic thermal conductance presents a cubic relation to the temperature [43,44]. Thus, at low temperature, we focus on the electronic thermal conductance.

III. HALF-QUANTIZED THERMAL CONDUCTANCE PLATEAU

First, we study the thermal transport properties of the hybrid QAHI-TSC-QAHI junction. The exchange field $M_{\mathrm{QAHI}}=0.25$ for $M_z>0$ ($M_{\mathrm{QAHI}}=-0.25$ for $M_z<0$) and chemical potential $\mu_{\mathrm{QAHI}}=0$ in QAHI. That is, there is only one quantum channel injecting/ejecting in the QAHI leads. The pairing potential $\Delta^t=\Delta$ and $\Delta^b=0$ in the central TSC. Figure 3(a) shows T, T_{CAR}, and T_{LAR} for the incident energy $E=0.005$ as functions of exchange field M_z of TSC. When the incident energy E is within the bulk gap, the transport behavior is determined by the chiral edge states. We first discuss the exotic case when the TSC is in the $\mathcal{N}=1$ phase so that a single CMF lives along the boundary of $\mathcal{C}=1$ QAHI and $\mathcal{N}=1$ TSC. Consider an incident electron propagating along the mode α_1 indicated by the red arrow from left QAHI lead [see Fig. 1(a)]; this electron propagates along the upper chiral edge state. When it reaches the QAHI-TSC interface, the incident electron splits into the two Majorana fermions γ_1 and γ_2, i.e., $\alpha_1=1/\sqrt{2}(\gamma_1+i\gamma_2)$. γ_1 propagates along the QAHI-TSC interface and returns back to the left terminal. γ_2 directly propagates to the right terminal [see Fig. 1(a)], i.e., $\gamma_1\to 1/\sqrt{2}(\beta_1+\beta_1^\dagger)$ and $\gamma_2\to 1/i\sqrt{2}(\beta_2-\beta_2^\dagger)$. This indicates that, for the incident mode α_1, the four scattering processes (normal tunneling T, T_{CAR}, T_{LAR} and normal reflection) have the same probability [15,17–19,22], i.e., $T=T_{CAR}=T_{LAR}=1/4$ holds the plateau of transport coefficients around $M_z=0.15$ in Fig. 3(a). This leads to the

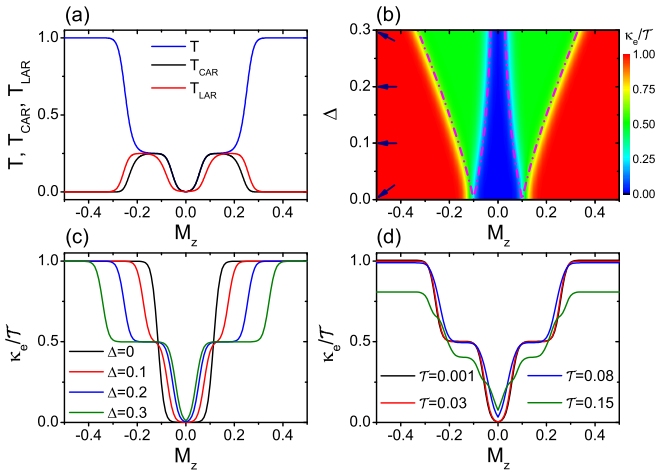

FIG. 3. Thermal transport properties in a QAHI-TSC-QAHI nanoribbon junction. The pairing potential $\Delta^t = 0.2$ and $\Delta^b = 0$ and M_z represents the exchange field in TSC. The exchange field $M_{\rm QAHI} = 0.25$ for $M_z > 0$ ($M_{\rm QAHI} = -0.25$ for $M_z < 0$) and chemical potential $\mu_{\rm QAHI} = 0$ in QAHI. (a) T, T_{CAR}, and T_{LAR} as functions of exchange field M_z in TSC with the incident electron energy $E = 0.005$. Panel (b) shows $\kappa_e/\mathcal{T}$ (in units of $\pi^2 k_B^2/3h$) distribution with temperature $\mathcal{T} = 0.03$, $\Delta^t = \Delta$. The magenta dashed dotted lines represent the boundaries of the superconducting phase diagram with $\mp\Delta \cdot M_z = M_z^2 + m_0^2$ [15]. (c) $\kappa_e/\mathcal{T}$ vs the function of M_z in TSC with $\Delta^t = \Delta$ ($\Delta = 0, 0.1, 0.2, 0.3$). Panel (d) plots $\kappa_e/\mathcal{T}$ as the function of M_z in TSC with temperature $\mathcal{T} = 0.001, 0.03, 0.08, 0.15$.

half-quantized electric conductance plateau, $G = \frac{1}{2}e^2/h$, as pointed out in the literature [15,25]. Besides, when the increasing M_z ($M_z > 0$) drives TSC into the $\mathcal{N} = 2$ phase, there are two CMFs, topologically equivalent to one electron. So the injecting electron from the left QAHI entirely transmits into the right QAHI; see the trajectory shown in Fig. 1(d). This leads to the $T = 1$ and $T_{CAR} = T_{LAR} = 0$ when $M_z > 0.3$ in Fig. 3(a) and corresponds to an integer quantized conductance $G = e^2/h$.

For thermal transport, the thermal conductance κ_e defined in Eq. (12) only depends on the normal tunneling T and crossed Andreev reflection T_{CAR}. At relatively low temperature, electrons participate thermal transport within a narrow energy range, where T and T_{CAR} are constant; the formula of κ_e is simplified as $\kappa_e/\mathcal{T} = (T + T_{CAR})\frac{\pi^2 k_B^2}{3h}$. In our design of the QAHI-TSC-QAHI junction, what contributes to nonzero T and T_{CAR} is only the CMF in the TSC region. $T = T_{CAR} = 1/4$ for $M_z = 0.15$ in Fig. 3(a) indicates that there is a single Majorana edge state residing at the edge of TSC. A single CMF is equivalent to half an ordinary fermion and will contribute to half a quantized thermal conductance. $T = 1$, $T_{CAR} = 0$ when $M_z > 0.3$ in Fig. 3(a) indicates that there are two CMFs existing on boundaries. Two CMFs contribute a quantized thermal conductance. Due to the Chern number $\mathcal{N}$ of TSC equal to the number of CMF edge modes, thus $\kappa_e/\mathcal{T} = \frac{|\mathcal{N}|}{2}\frac{\pi^2 k_B^2}{3h}$. This means that $\kappa_e/\mathcal{T}$ can reveal the information of the CMFs and the presence of the CMF in the central TSC regions is confirmed with aids of the quantized thermal conduction plateau.

The color plot of $\kappa_e/\mathcal{T}$ with quantized values in Fig. 3(b) indeed distinguishes different phases of TSC with parameters Δ and M_z at temperature $\mathcal{T} = 0.03$. For a clear description, we take $\Delta = 0, 0.1, 0.2, 0.3$ (marked with small arrows) and plot $\kappa_e/\mathcal{T}$ as functions of M_z in Fig. 3(c). Figure 3(c) shows $\kappa_e/\mathcal{T}$ plateaus change from 1 to 1/2 to 0 to 1/2 to 1, indicating the Chern number of the superconducting of the central region varying $\mathcal{N} = -2 \to -1 \to 0 \to 1 \to 2$ as exchange field M_z increases. Besides the case with $\Delta = 0$ only corresponding to the $\mathcal{N} = \pm 2$ and $\mathcal{N} = 0$ phase, $\kappa_e/\mathcal{T}$ curves with nonzero Δ (0.1, 0.2, 0.3) all present the 1/2 quantized plateau, that is, the half-quantized thermal conductance of a single CMF. These half-integer quantized thermal conductance plateaus can serve as a reliable signature of topologically protected chiral edge states of charge-neutral Majorana fermions. Next, we investigate the effect of temperature on the quantized thermal conductance plateaus. Figure 3(d) displays $\kappa_e/\mathcal{T}$ versus M_z for different temperatures. We find that, when the temperature is low, the $k_B\mathcal{T}$ is much smaller than the induced bulk gap Δ_p of TSC [bulk gap $\Delta_p \approx 0.05$; see Fig. 2(e)] and the quantized thermal conductance plateau is maintained well over a certain temperature range. As the temperature increases, the quantized plateau still exists even if the $k_B\mathcal{T}$ is larger than the Δ_p of TSC.

Now, we study the thermal transport properties in a metal-TSC-metal ribbon structure. In fact, compared with the QAHI-TSC-QAHI nanoribbon structure, metal leads are very common and easier to fabricate in experiments. In this paper, we tune the QAH phase into the metallic phase with the exchange field $M_{\rm QAHI} = 0.25$ for $M_z > 0$ ($M_{\rm QAHI} = -0.25$ for $M_z < 0$) and chemical potential $\mu_{\rm QAHI} = 0.8$ and 1.5 ($|\mu_{\rm QAHI}| > |m_0|$) in QAHI. The electric conductance of the metal-TSC-metal junction is usually very large, because Cooper pairs in TSC can carry the electric current. Here we focus on the thermal transport through the metal-TSC-metal junction, which cannot be carried by the Cooper pairs. Figure 4(a) shows T, T_{CAR}, and T_{LAR} as functions of exchange field M_z in TSC. Figure 4(b) plots $\kappa_e/\mathcal{T}$ versus the exchange field M_z in TSC with $\Delta = 0$, 0.1, 0.2, and 0.3 at the temperature $\mathcal{T} = 0.03$.

With metal leads connected to the central TSC region, the injected electrons from leads can be reflected as electrons or holes (T_{LAR}), or transmitted as electrons (T) or holes (T_{CAR}). Different from the QAHI-TSC-QAHI structure, there are multiple channels in normal metal so that the local Andreev reflection coefficient can be over 1 even at the $\mathcal{N} = 1$ TSC as shown in Fig. 4(a). Thus the two-terminal electric conductance is very large and does not present the quantized value as usual. However, this obstacle can be overcome in the thermal transport measurement. Figure 4(b) shows the well preserved half-integer plateau of $\kappa_e/\mathcal{T}$ versus M_z in the metal-TSC-metal structure. Since the thermal conductance is related to the T and T_{CAR}, the local Andreev process does not affect $\kappa_e/\mathcal{T}$. Therefore, in the metal-TSC-metal structure, when the Chern number of TSC varies from $\mathcal{N} = -2 \to -1 \to 0 \to 1 \to 2$, the thermal conductance plateau also changes: $1 \to 1/2 \to 0 \to 1/2 \to 1$ [see Fig. 4(b)]. In this case, thermal conductance κ_e has a clear advantage in revealing the chiral

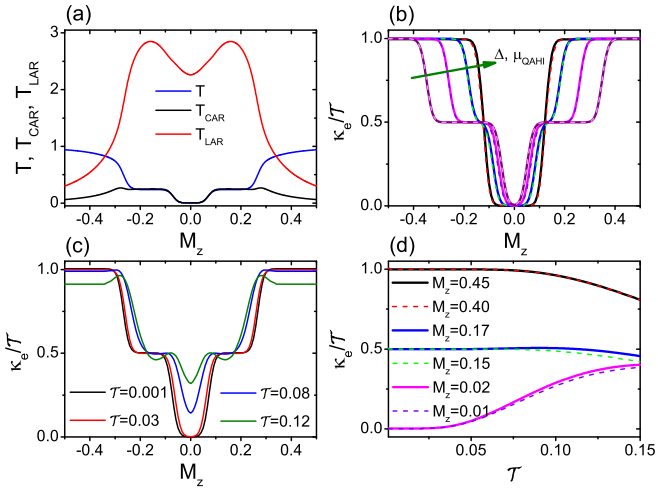

FIG. 4. Thermal transport properties in a hybrid metal-TSC-metal ribbon structure. The pairing potential $\Delta^t = 0.2$ and $\Delta^b = 0$ and M_z represents the exchange field in TSC. The exchange field $M_{\rm QAHI} = 0.25$ for $M_z > 0$ ($M_{\rm QAHI} = -0.25$ for $M_z < 0$) and chemical potential $\mu_{\rm QAHI} = 0.8$ in QAHI. (a) T, T_{CAR}, and T_{LAR} as functions of exchange field M_z in TSC with $E = 0.005$. Panel (b) shows $\kappa_e/\mathcal{T}$ vs M_z in TSC with temperature $\mathcal{T} = 0.03$, $\mu_{\rm QAHI} = 0.8$ (solid line), and $\mu_{\rm QAHI} = 1.5$ (dashed lines), along the direction of the green arrow $\Delta^t = \Delta = 0.3, 0.2, 0.1, 0$ in turn. Panel (c) plots $\kappa_e/\mathcal{T}$ vs the function of M_z in TSC with temperature $\mathcal{T} = 0.001, 0.03, 0.08, 0.12$. Panel (d) plots $\kappa_e/\mathcal{T}$ vs temperature $\mathcal{T}$. Exchange field $M_z = 0.45$, 0.40, 0.17, 0.15, 0.02, and 0.01 in TSC, respectively.

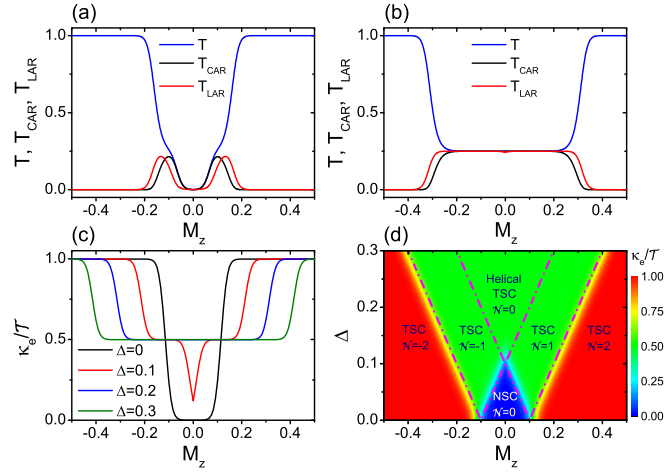

FIG. 5. Thermal transport properties of QAHI-TSC-QAHI structure. The pairing potential $\Delta^t = -\Delta^b = \Delta$ and M_z represents the exchange field in TSC. The exchange field $M_{\rm QAHI} = 0.25$ for $M_z > 0$ ($M_{\rm QAHI} = -0.25$ for $M_z < 0$) and chemical potential $\mu_{\rm QAHI} = 0$ in QAHI. T, T_{CAR}, and T_{LAR} vs exchange field M_z in TSC with the energy $E = 0.005$ of the incident electron. $\Delta = 0.05$ for panel (a) and $\Delta = 0.2$ for panel (b). (c) $\kappa_e/\mathcal{T}$ as the function of M_z in TSC with $\Delta = 0, 0.1, 0.2, 0.3$. Panel (d) shows $\kappa_e/\mathcal{T}$ distribution with the temperature $\mathcal{T} = 0.03$. The magenta dashed dotted lines represent the boundaries of the superconducting phase diagram with $M_z^2 - \Delta^2 = m_0^2$ [15].

Majorana edge state that cannot be detected by the electrical conductance. In addition, the thermal conductance plateau is independent of the chemical potential $\mu_{\rm QAHI}$ of QAHI. In other words, when the TSC pairing potential $\Delta^t = \Delta$ is the same in Fig. 4(b), the thermal conductance plateau curves of $\mu_{\rm QAHI} = 0.8$ and $\mu_{\rm QAHI} = 1.5$ coincide.

Figures 4(c) and 4(d) show the effect of temperature on the thermal conductance plateau. The change of thermal conductance with exchange field M_z in TSC at different temperature is shown in Fig. 4(c) and the change of thermal conductance with temperature $\mathcal{T}$ at different exchange field M_z is shown in Fig. 4(d). Similar to the conclusion of Fig. 3(d), we also find that the plateau maintains well within a certain temperature range.

IV. HELICAL TOPOLOGICAL SUPERCONDUCTOR

In this section, we focus on the thermal transport properties of helical TSC. We adopt the hybrid QAHI-TSC-QAHI (see Fig. 5) and metal-TSC-metal structure (see Fig. 6). We tune the QAH phase into the metallic phase with $M_{\rm QAHI} = 0.25$ for $M_z > 0$ ($M_{\rm QAHI} = -0.25$ for $M_z < 0$) and chemical potential $\mu_{\rm QAHI} = 0.8$ ($|\mu_{\rm QAHI}| > |m_0|$) in QAHI. When the pairing potentials $\Delta^t = -\Delta^b = \Delta$ in TSC, a helical TSC forms [15,45–50]. The edges of helical TSC are composed of two chiral Majorana edge modes with opposite chiralities, also known as the Majorana Kramers pair. So far, helical TSC has not been observed in experiments [15,49,50].

Figures 5(a) and 5(b) plot the transmission coefficients (T, T_{CAR}, and T_{LAR}) in the QAHI-TSC-QAHI structure as functions of the exchange field M_z for different pairing gap Δ ($\Delta = 0.05, 0.2$). Figure 5(c) shows $\kappa_e/\mathcal{T}$ versus the exchange field M_z with $\Delta^t = -\Delta^b = \Delta = 0, 0.1, 0.2, 0.3$ under temperature $\mathcal{T} = 0.03$ and Fig. 5(d) plots $\kappa_e/\mathcal{T}$ distribution. Analogously, in metal-TSC-metal structure, Fig. 6(a) plots T, T_{CAR}, and T_{LAR} as functions of the exchange field M_z with $\Delta = 0.2$, Fig. 6(b) shows $\kappa_e/\mathcal{T}$ versus the exchange field M_z with $\Delta^t = -\Delta^b = \Delta = 0, 0.1, 0.2, 0.3$ under temperature $\mathcal{T} = 0.03$, Fig. 6(c) displays $\kappa_e/\mathcal{T}$ versus M_z for different temperatures, and Fig. 6(d) plots $\kappa_e/\mathcal{T}$ distribution.

In Fig. 5(a), at fixed $\Delta = 0.05$, the Chern number of TSC is $\mathcal{N} = \pm 2$ for $|M_z| > 0.15$ and two chiral Majorana edge states propagate along the system boundaries; $\mathcal{N} = \pm 1$ for $0.15 > |M_z| > 0.05$, and a single Majorana edge state is on the boundary; $\mathcal{N} = 0$ for $|M_z| < 0.05$, and there is no Majorana edge state [50]. This is completely similar to Fig. 2(a), so the thermal conductance plateau varies $1 \to 1/2 \to 0 \to 1/2 \to 1$ [see Figs. 5(c) and 5(d)]. In Fig. 5(b), we take $\Delta = 0.2$ and $m_0 = -0.1$. For $|m_0| + \Delta < |M_z|$ (i.e., $0.3 < |M_z|$), the Chern number of TSC is $\mathcal{N} = \pm 2$; for $-|M_z| - \Delta < m_0 < -||M_z| - \Delta|$ (i.e., $0.1 < |M_z| < 0.3$), the Chern number of TSC is $\mathcal{N} = \pm 1$ [50]. These two cases are completely similar to Fig. 5(a). However, for $|m_0| < \Delta - |M_z|$ ($|M_z| < 0.1$), a helical TSC with Chern number $\mathcal{N} = 0$ appears [see the markings in Fig. 5(d)]. In this helical TSC phase, a pair of Majorana edge states with opposite chirality exist along the boundary of the central TSC region. One branch propagates in the clockwise direction and the other branch propagates in the counterclockwise direction, similar to the quantum spin

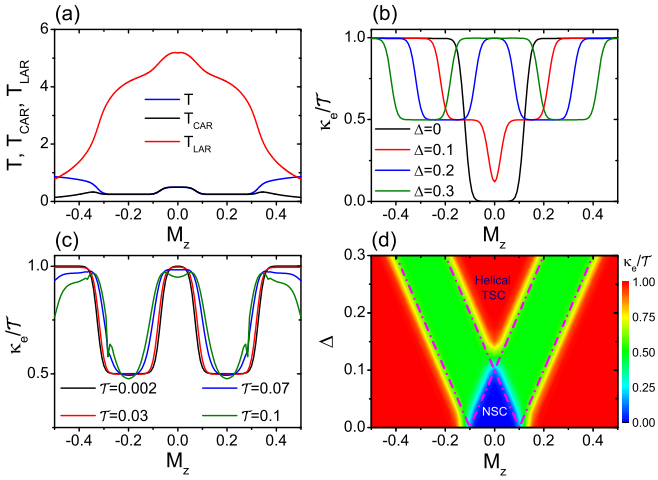

FIG. 6. Thermal transport properties of metal-TSC-metal structure. The pairing potential $\Delta^t = -\Delta^b = \Delta$ and M_z represent the exchange field in TSC. The exchange field $M_{\rm QAHI} = 0.25$ for $M_z > 0$ ($M_{\rm QAHI} = -0.25$ for $M_z < 0$) and chemical potential $\mu_{\rm QAHI} = 0.8$ in QAHI. (a) T, T_{CAR}, and T_{LAR} vs exchange field M_z in TSC with $\Delta = 0.2$; the incident electron energy $E = 0.005$. (b) $\kappa_e/\mathcal{T}$ vs the function of M_z in TSC with $\Delta = 0, 0.1, 0.2, 0.3$. Panel (c) plots $\kappa_e/\mathcal{T}$ vs the function of M_z in TSC with $\Delta = 0.2$ and the temperature $\mathcal{T} = 0.002, 0.03, 0.07, 0.1$. Panel (d) shows $\kappa_e/\mathcal{T}$ distribution with the temperature $\mathcal{T} = 0.03$. The magenta dashed dotted lines represent the boundaries of the superconducting phase diagram with $M_z^2 - \Delta^2 = m_0^2$ [15].

Hall insulator [50]. The mode that contributes to the thermal conductance is the Majorana edge mode at the boundary of the topological superconductor, which enters from the lead of QAHI on the left and flows out from the right. This is equivalent to ejecting half of an ordinary fermion. The half ordinary fermion contributes the half quantized thermal conductance, so a half-integer quantized thermal conductance plateau forms [see Figs. 5(c) and 5(d)].

When we use metallic leads instead of the QAHI leads, the most obvious difference is that the thermal conductance plateau exhibits an integer quantized plateau in the metal-TSC-metal structure as the helical TSC is produced [see Figs. 6(c) and 6(d)]. Since there are multiple channels in normal metals, electrons are incident on the central TSC area. For helical TSC, there is a single Majorana bound state at each upper and lower edge to carry heat, so the normal tunneling T and the crossed Andreev reflection coefficient T_{CAR} are $1/2$ other than $1/4$ [see Fig. 6(a)]. A pair of Majorana bound states residing at the edge is equivalent to ejecting an ordinary fermion and an ordinary fermion will contribute a quantized thermal conductance. So, we will obtain an integer quantized thermal conductance plateau. As shown in Fig. 6(c), when the background temperature $\mathcal{T}$ is low, e.g, $\mathcal{T} = 0.002$, the thermal conductance shows the integer and half-integer quantized plateaus, which correspond to the helical and chiral TSC phases, respectively. With the increase of the temperature $\mathcal{T}$, these quantized thermal conductance plateaus can well keep as $k_B\mathcal{T}$ being lower than the induced bulk gap of the TSC (approximately 0.03), but they are gradually destroyed at $k_B\mathcal{T}$ larger than the induced bulk gap. We can use the jump from $1/2 \to 1$ of the thermal conductance plateau to identify the helical Majorana edge state, which provides a useful tool for experimentally identifying the helical TSC.

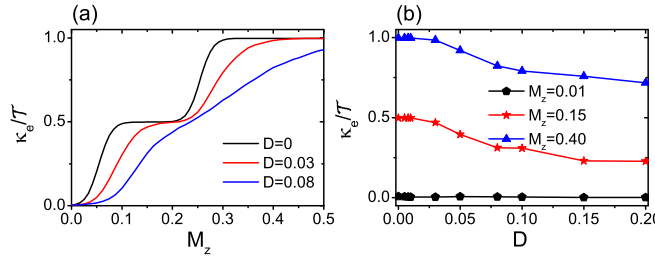

FIG. 7. Effects of disorder on thermal transport properties in QAHI-TSC systems. The pairing potential $\Delta^t = 0.2$ and $\Delta^b = 0$ and M_z represents the exchange field in TSC. The exchange field $M_{\rm QAHI} = 0.25$ and chemical potential $\mu_{\rm QAHI} = 0$ in QAHI. (a) $\kappa_e/\mathcal{T}$ as the function of exchange field M_z in TSC at the different disorder strength D ($D = 0, 0.03, 0.08$) with temperature $\mathcal{T} = 0.03$. (b) $\kappa_e/\mathcal{T}$ vs disorder strength D with exchange field $M_z = 0.01, 0.15$, and 0.40 in TSC.

V. EFFECT OF DISORDER

Up to now, we have shown that the half-integer thermal conductance plateau occurs in the pure QAHI-TSC and metal-TSC systems. Since impurities and disorder exist inevitably in real materials, next, let us investigate the effect of disorder on the thermal conductance plateau.

We introduce the Anderson-type disorder in the central TSC region of a hybrid QAHI-TSC structure. Based on the Hamiltonian in Eq. (2), the Anderson-type disorder is introduced by an additional term to the on-site energy. $D_i\tau_0\sigma_0$ is added to the diagonal part $H_{\rm QAHI}(p)$ and $-D_i\tau_0\sigma_0$ is added to $-H^*_{\rm QAHI}(-p)$. D_i is uniformly distributed in the interval $[-D/2, D/2]$ with the disorder strength D. We take the exchange field $M_{\rm QAHI} = 0.25$ and chemical potential $\mu_{\rm QAHI} = 0$ in QAHI and the pairing potentials $\Delta^t = 0.2$ and $\Delta^b = 0$ in TSC. In the central TSC region, disorder of possessive points is random and independent of each other. With each value of disorder strength D, thermal conductance κ_e is averaged up to 40 configurations.

Figure 7(a) shows $\kappa_e/\mathcal{T}$ with different disorder strength at temperature $\mathcal{T} = 0.03$. Figure 7(b) shows $\kappa_e/\mathcal{T}$ versus the disorder strength D for different exchange field M_z in TSC with $M_z = 0.01$, 0.15, and 0.40. The half-integer plateau of $\kappa_e/\mathcal{T}$ preserves well with moderate strength of disorder, $D = 0.03$, which is half of the induced gap Δ_p of TSC. With the increase of D, the plateaus of $\kappa_e/\mathcal{T}$ are gradually destroyed (e.g., $D = 0.08$) (see Fig. 7). Thus, for the experimental observation of a half-quantized thermal conductance plateau, disorder can exist in the sample but should not be too strong to close the gap of TSC.

VI. DISCUSSIONS AND CONCLUSIONS

As compared with the experimental materials, the Fermi velocity is estimated as about $\hbar v_F \sim 260$ meV nm in the Cr-(Bi, Sb)$_2$Te$_3$ films [51]. Then we choose the length unit as 0.17 μm such that the dimensionless lattice constant $a = 0.75$

corresponds to about 0.17 μm $\times$ 0.75 $\approx$ 0.13 μm. The dimensionless superconducting gap, e.g., $\Delta = 0.2$, corresponds to a real value $\Delta \sim 0.4$ meV, which is achievable because the proximity induced superconducting gap of Bi_2Se_3 films on the $NbSe_2$ substrate can reach $\Delta = 0.5$ meV even at 4.2 K [8,15]. The dimensionless mass gap $m_0 = -0.1$ corresponds to a real value $|m_0| \sim 0.2$ meV, which is in the same amplitude of the QAHE in the Cr-$(Bi, Sb)_2Te_3$ films. Also, the size of each TSC region, (100a, 80a), corresponds to (13 μm, 10.4 μm), which is comparable to the recent experimental device [25].

From the experimental perspective, we discuss the feasibility of our proposal. As to the experimental technique, recent experiments have utilized the thermal transport method to confirm the theoretical conjecture of physical systems, such as the heavy-fermion superconductor [31] and the quantum Hall system without/with strong correlations [52,53]. These experiments could be performed at a temperature as low as 10 mK, within the requirement of QAHE. As to the effect of measurement to the quantum regime, on the one hand, the QAHI/TSC owns the topologically protected bulk gap, which is robust against local perturbation, such as the shape, size, and impurities of specific devices. On the other hand, we have shown that both the QAHI and the normal metal can be used as detecting leads, as would not affect the thermal transport signature.

In summary, a half-integer quantized thermal conductance plateau is found in the hybrid QAHI(metal)-TSC ribbon system when the $\mathcal{N} = \pm 1$ TSC phase is realized. The quantized plateau can be maintained well in a certain temperature range and in moderate disorder, but it will be destroyed with the increase of temperature $\mathcal{T}$ and disorder D. The half-integer quantized thermal conductance plateau can also serve as reliable evidence of the existence of Majorana fermions in experiments.

ACKNOWLEDGMENTS

This work was financially supported by NSF-China (Grants No. 12164038 and No. 11921005), National Key R&D Program of China (Grant No. 2017YFA0303301), the Strategic Priority Research Program of Chinese Academy of Sciences (Grant No. XDB28000000)), and Beijing Municipal Science & Technology Commission (Grant No. Z191100007219013), the Scientific Research Project of Shihezi University (Grant No. RCZK2021B04).

[1] E. Majorana, Nuovo Cimento **14**, 171 (1937).
[2] S. R. Elliott and M. Franz, Rev. Mod. Phys. **87**, 137 (2015).
[3] C. W. J. Beenakker, Annu. Rev. Condens. Matter Phys. **4**, 113 (2013).
[4] X.-L. Qi and S.-C. Zhang, Rev. Mod. Phys. **83**, 1057 (2011).
[5] A. R. Akhmerov, J. Nilsson, and C. W. J. Beenakker, Phys. Rev. Lett. **102**, 216404 (2009).
[6] L. Fu and C. L. Kane, Phys. Rev. Lett. **102**, 216403 (2009).
[7] S. B. Chung, X.-L. Qi, J. Maciejko, and S.-C. Zhang, Phys. Rev. B **83**, 100512(R) (2011).
[8] V. Mourik, K. Zuo, S. M. Frolov, S. R. Plissard, E. P. A. M. Bakkers, and L. P. Kouwenhoven, Science **336**, 1003 (2012).
[9] Z. Wang, *Topological Quantum Computation* (American Mathematical Society, Santa Barbara, 2010).
[10] C. Nayak, S. H. Simon, A. Stern, M. Freedman, and S. Das Sarma, Rev. Mod. Phys. **80**, 1083 (2008).
[11] S. Das Sarma, M. Freedman, and C. Nayak, Phys. Today **59**(7), 32 (2006).
[12] D. Aasen, M. Hell, R. V. Mishmash, A. Higginbotham, J. Danon, M. Leijnse, T. S. Jespersen, J. A. Folk, C. M. Marcus, K. Flensberg, and J. Alicea, Phys. Rev. X **6**, 031016 (2016).
[13] A. Stern and E. Berg, Phys. Rev. Lett. **122**, 107701 (2019).
[14] X.-L. Qi, T. L. Hughes, and S.-C. Zhang, Phys. Rev. B **82**, 184516 (2010).
[15] J. Wang, Q. Zhou, B. Lian, and S.-C. Zhang, Phys. Rev. B **92**, 064520 (2015).
[16] B. Lian, J. Wang, and S.-C. Zhang, Phys. Rev. B **93**, 161401(R) (2016).
[17] Y.-T. Zhang, Z. Hou, X. C. Xie, and Q.-F. Sun, Phys. Rev. B **95**, 245433 (2017).
[18] Y.-F. Zhou, Z. Hou, Y.-T. Zhang, and Q.-F. Sun, Phys. Rev. B **97**, 115452 (2018).
[19] Y.-F. Zhou, Z. Hou, P. Lv, X. C. Xie, and Q.-F. Sun, Sci. China: Phys., Mech. Astron. **61**, 127811 (2018).
[20] B. Lian, J. Wang, X.-Q. Sun, A. Vaezi, and S.-C. Zhang, Phys. Rev. B **97**, 125408 (2018).
[21] Y.-H. Li, J. Liu, H. Liu, H. Jiang, Q.-F. Sun, and X. C. Xie, Phys. Rev. B **98**, 045141 (2018).
[22] Q. Yan, Y.-F. Zhou, and Q.-F. Sun, Phys. Rev. B **100**, 235407 (2019).
[23] B. Lian, X.-Q. Sun, A. Vaezi, X.-L. Qi, and S.-C. Zhang, Proc. Natl. Acad. Sci. USA **115**, 10938 (2018).
[24] Y.-F. Zhou, Z. Hou, and Q.-F. Sun, Phys. Rev. B **99**, 195137 (2019).
[25] Q. L. He, L. Pan, A. L. Stern, E. C. Burks, X. Che, G. Yin, J. Wang, B. Lian, Q. Zhou, E. S. Choi, K. Murata, X. Kou, Z. Chen, T. Nie, Q. Shao, Y. Fan, S.-C. Zhang, K. Liu, J. Xia, and K. L. Wang, Science **357**, 294 (2017).
[26] M. Kayyalha, D. Xiao, R. Zhang, J. Shin, J. Jiang, F. Wang, Y.-F. Zhao, R. Xiao, L. Zhang, K. M. Fijalkowski, P. Mandal, M. Winnerlein, C. Gould, Q. Li, L. W. Molenkamp, M. H. W. Chan, N. Samarth, and C.-Z. Chang, Science **367**, 64 (2020).
[27] C.-Z. Chen, J. J. He, D.-H. Xu, and K. T. Law, Phys. Rev. B **96**, 041118(R) (2017).
[28] W. Ji and X.-G. Wen, Phys. Rev. Lett. **120**, 107002 (2018).
[29] Y. Huang, F. Setiawan, and J. D. Sau, Phys. Rev. B **97**, 100501(R) (2018).
[30] C.-Z. Chen, J. J. He, D.-H. Xu, and K. T. Law, Phys. Rev. B **98**, 165439 (2018).
[31] S. Jezouin, F. D. Parmentier, A. Anthore, U. Gennser, A. Cavanna, Y. Jin, and F. Pierre, Science **342**, 601 (2013).
[32] M. Banerjee, M. Heiblum, V. Umansky, D. E. Feldman, Y. Oreg, and A. Stern, Nature (London) **559**, 205 (2018).
[33] Y. Shimizu, A. Yamakage, and K. Nomura, Phys. Rev. B **91**, 195139 (2015).

[34] Q. Yan, Y.-F. Zhou, and Q.-F. Sun, Chin. Phys. B **29**, 097401 (2020).
[35] N.-X. Yang, Q. Yan, and Q.-F. Sun, Phys. Rev. B **102**, 245412 (2020).
[36] W. Long, Q.-F. Sun, and J. Wang, Phys. Rev. Lett. **101**, 166806 (2008).
[37] N.-X. Yang, Z. Hou, and Q.-F. Sun, Phys. Rev. B **101**, 035418 (2020).
[38] Q.-F. Sun, J. Wang, and T.-H. Lin, Phys. Rev. B **59**, 3831 (1999).
[39] Q.-F. Sun, P. Yang, and H. Guo, Phys. Rev. Lett. **89**, 175901 (2002).
[40] G. Michałek, M. Urbaniak, B. R. Bułka, T. Domański, and K. I. Wysokiński, Phys. Rev. B **93**, 235440 (2016).
[41] S. Y. Hwang, R. López, and D. Sánchez, Phys. Rev. B **94**, 054506 (2016).
[42] Q.-F. Sun and X. C. Xie, J. Phys.: Condens. Matter **21**, 344204 (2009).
[43] P. G. Klemens, in *Solid State Physics*, edited by F. Seitz and D. Turnbull (Academic, New York, 1958), Vol. 7, p. 1.
[44] J. Yang, in *Thermal Conductivity: Theory, Properties and Applications*, edited by T. M. Tritt (Kluwer Academic, New York, 2004), pp. 1–20.
[45] F. Zhang, C. L. Kane, and E. J. Mele, Phys. Rev. Lett. **111**, 056402 (2013).
[46] J. Klinovaja, A. Yacoby, and D. Loss, Phys. Rev. B **90**, 155447 (2014).
[47] J. Wang, Phys. Rev. B **94**, 214502 (2016).
[48] C.-X. Liu and B. Trauzettel, Phys. Rev. B **83**, 220510(R) (2011).
[49] Y. Huang and C.-K. Chiu, Phys. Rev. B **98**, 081412(R) (2018).
[50] Q. Li, Y. Han, K. Zhang, Y.-T. Zhang, J.-J. Liu, and Z. Qiao, Phys. Rev. B **102**, 205402 (2020).
[51] C.-Z. Chang, J. Zhang, X. Feng, J. Shen, Z. Zhang, M. Guo, K. Li, Y. Ou, P. Wei, L.-L. Wang, Z.-Q. Ji, Y. Feng, S. Ji, X. Chen, J. Jia, X. Dai, Z. Fang, S.-C. Zhang, K. He, Y. Wang *et al.*, Science **340**, 167 (2013).
[52] G. Seyfarth, J. P. Brison, G. Knebel, D. Aoki, G. Lapertot, and J. Flouquet, Phys. Rev. Lett. **101**, 046401 (2008).
[53] M. Banerjee, M. Heiblum, A. Rosenblatt, Y. Oreg, D. E. Feldman, A. Stern, and V. Umansky, Nature (London) **545**, 75 (2017).